with recently reported forms of organic electronics, in which certain constituent materials are water-soluble (*1*–*3*), or with simple nontransient transistors formed on bioresorbable substrates (*4*).

Figure 1, A and B, and fig. S1 provide images and schematic diagrams of a demonstration platform. All of the components, ranging from the inductors, capacitors, resistors, diodes, transistors, interconnects, and crossovers, to the substrate and encapsulation, disintegrate and dissolve when immersed in deionized (DI) water (Fig. 1C). This example uses magnesium (Mg) for the conductors, magnesium oxide (MgO) (silicon dioxide, SiO_2, is also possible) for the dielectrics, monocrystalline silicon (Si) nanomembranes (NMs) for the semiconductors, and silk (which is water-soluble and enzymatically degradable) (*4*, *5*) for the substrate and packaging material. The fabrication of systems such as this one involves a combination of transfer printing (Si NMs) (*6*), physical vapor deposition through fine-line stencil masks (Mg, MgO, and SiO_2), and solution-casting (silk). More details on sample preparation can be found in (*6*). As adhesion promoters for Mg, we used MgO in certain cases and ultrathin layers of Ti in others. Device yields without the Ti are 70 to ~80% with evaporated Mg and >90% with sputtered Mg.

The chemical reactions responsible for the dissolution of each material appear in Fig. 1D. The Si NMs and layers of SiO_2 are particularly important because of their essential roles in high-performance transistors, diodes, photodetectors, solar cells, temperature sensors, strain gauges, and other semiconductor devices. The NM geometry is critical because it enables high-performance devices and planar architectures, minimizes the amount of material that must be consumed during the transient step, and provides mechanics and processing options that are favorable for heterogeneous integration onto substrates such as silk (*4*), as well as elastomers that can provide modulus-matched interfaces with the body (*7*). A typical transistor described here requires less than ~1 μg of Si, which can be dissolved in as little as 30 μl of biofluid (*8*).

Figure 2A presents atomic force micrographs of a Si NM (3 × 3 μm) with a thickness of 70 nm, collected at different stages of dissolution in phosphate-buffered saline (PBS; pH of 7.4) at 37°C, to simulate transience by bioresorption (see figs. S2 and S3A for additional data). The dissolution involves hydrolysis to form $Si(OH)_4$ (*9*), according to $Si + 4\ H_2O \leftrightarrow Si(OH)_4 + 2\ H_2$, where SiO_2 can sometimes be involved as an intermediate (*10*). The simplest model of the kinetics, which depends strongly on pH, considers a constant reaction rate at the water/Si NM interface (*11*). The results capture experimental observations at both body temperature (37°C) (Fig. 2C) and room temperature (25°C) (fig. S3A) for a dissolution rate of 4.5 nm/day and 2 nm/day, respectively, consistent with Arrhenius scaling (*12*).

Mechanisms involving diffusion into the materials can be important for Mg and MgO deposited by electron-beam evaporation and SiO_2 formed by chemical vapor deposition, or as an intermediate in the hydrolysis of Si. In such cases, the kinetics can be described analytically using models of reactive diffusion (Fig. 2B) (*6*). The results quantitatively account for related behaviors in other materials for transient electronics, including those in Fig. 1 (*6*). Figure 2D presents a meander trace of Mg (150 nm) on a thin film of MgO (10 nm; adhesion promoter), in which the measured changes in resistance correlate well with those expected based on computed changes in thickness (Fig. 2E and fig. S4, A and B) (*6*). (Other examples appear in fig. S5.) This result connects a key electrical property to models of reactive diffusion, thereby suggesting the capacity to use such analytics in conjunction with established circuit simulators as a comprehensive design approach.

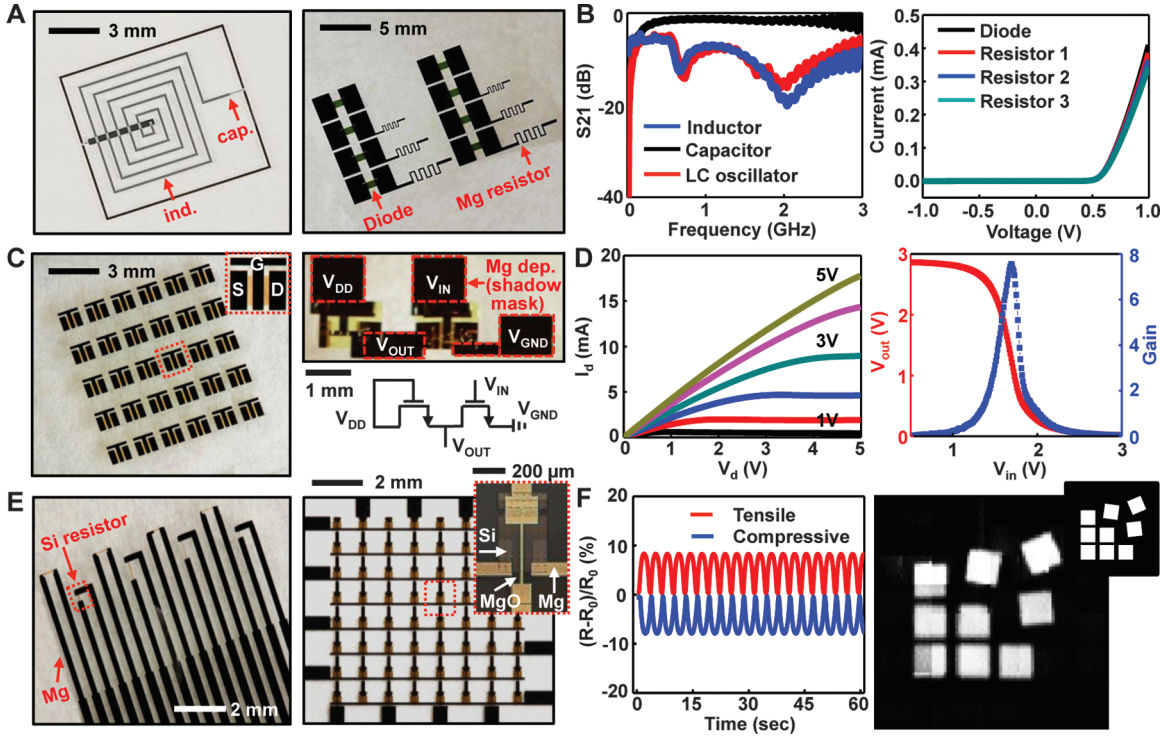

Fig. 3. Images and electrical properties of transient electronic components, circuits, and sensors, including simple integrated circuits and sensor arrays. (**A**) Image of an LC (inductor-capacitor) oscillator fabricated with Mg electrodes and MgO dielectric layers (left) and an array of Si NM diodes with serpentine Mg resistors (right). (**B**) Measurements of the S21 scattering parameter of an inductor (blue), capacitor (black), and LC oscillator (red) at frequencies up to 3 GHz (left). Current-voltage (*I-V*) characteristics of diodes connected to three different Mg resistors (right) are shown. (**C**) Images of an array of p-channel (left) MOSFETs and a logic gate (inverter; right) composed of n-channel MOSFETs. The MOSFETs use Mg source (S), drain (D), and gate (G) electrodes; MgO gate dielectrics; and Si NM semiconductors. The inverter uses Mg for interconnects and Au for source, drain, and gate electrodes, in a circuit configuration shown in the diagram. (**D**) *I-V* characteristics of a representative n-channel MOSFET [left, channel length (L_{ch}) and width (*W*) are 20 μm and 900 μm, respectively]. Transfer characteristic for the inverter (right, L_{ch} and *W* are 20 μm and 700 μm for the input transistor and 500 μm and 40 μm for the load transistor, respectively). The voltage gain is ~8. (**E**) Image of strain sensors based on Si NM resistors (left) and an addressable array of Si NM photodetectors with blocking diodes. In both cases, Mg serves as contact and interconnection electrodes and MgO as the dielectric. (**F**) Fractional change in resistance of a representative strain gauge as a function of time during cyclic loading (left). *R*, bent; R_0, flat. Bending induces tensile (red) and compressive (blue) strains uniaxially up to ~0.2%. Right, image of a logo collected with the photodetector array. The inset shows the logo design.

The transience times for NM-based electronic components can be extended, in controlled amounts, by adding transient encapsulating layers and packaging materials; they can be reduced by decreasing the critical dimensions or by physically structuring the materials in a way that accelerates dissolution by disintegration (fig. S6). Figure 2E and fig. S4 show results of measured transience in a serpentine resistor of Mg, encapsulated with different thicknesses of MgO and with combinations of MgO and overcoats of silk. Corresponding modeling results are also shown in (*6*). Silk is attractive for this purpose because its solubility in water can be programmed, over several orders of magnitude, through the control of crystallinity (*5*, *13*). Other biodegradable polymers can also be used, as shown in fig. S7.

Studies of transience at the device level are also important. Figure 2F shows examples of metal oxide semiconductor field-effect transistors (MOSFETs) formed using Si NMs, SiO_2 gate dielectrics, and Mg electrodes, with encapsulating layers of MgO and crystallized silk. The devices show two-stage kinetics in their functional transience. Immersion in DI water for up to ~90 hours causes negligible change in key device characteristics. Functional degradation then occurs in a relatively narrow time interval after this period of stable operation. The encapsulation defines the first time scale; the Mg electrodes define the second. The results demonstrate that the transience time can be engineered in a way that is decoupled from system- or device-level function.

These materials, fabrication techniques, and modeling tools can yield components for almost any type of transient electronic system, in CMOS designs. Figure 3 presents several examples, including additional details on MOSFETs similar to those in Fig. 2F, where both n- and p-channel operation is possible. The resulting electrical properties for an n-channel device include saturation and linear regime mobilities of 560 $cm^2/V{\cdot}s$ and 660 $cm^2/V{\cdot}s$, respectively, on/off ratios of $>10^5$, subthreshold slopes of 160 mV/dec [at drain voltage (V_d) = 0.1 V] and width-normalized current outputs of 0.34 mA/mm [at gate voltage (V_g) = 5 V]. These characteristics, as well as those of similar p-channel devices, compare favorably to the performance of counterparts formed on Si-on-insulator (SOI) wafers (*14*). [For the range of channel lengths investigated, contact resistances do not limit performance (fig. S8).] In all cases, the transience times of different elements in an integrated system can be controlled by use of varied thicknesses and/or stack compositions, or even via combination with nontransient materials. This last possibility is shown in a logic gate (inverter) in the righthand panels of Fig. 3, C and D, where a nontransient metal (Au) serves as source, drain, and gate electrodes for two transistors joined by transient Mg interconnects.

Many other classes of semiconductor devices and passive components are possible, with examples in Fig. 3 and figs. S9 and S10. The resistors and diodes can serve as temperature sensors; the latter can also be used in photodetectors and solar cells, as shown in Fig. 3 and fig. S10. The Si NM diode and Mg resistive temperature sensors show sensitivities of –2.23 mV/°C (change in

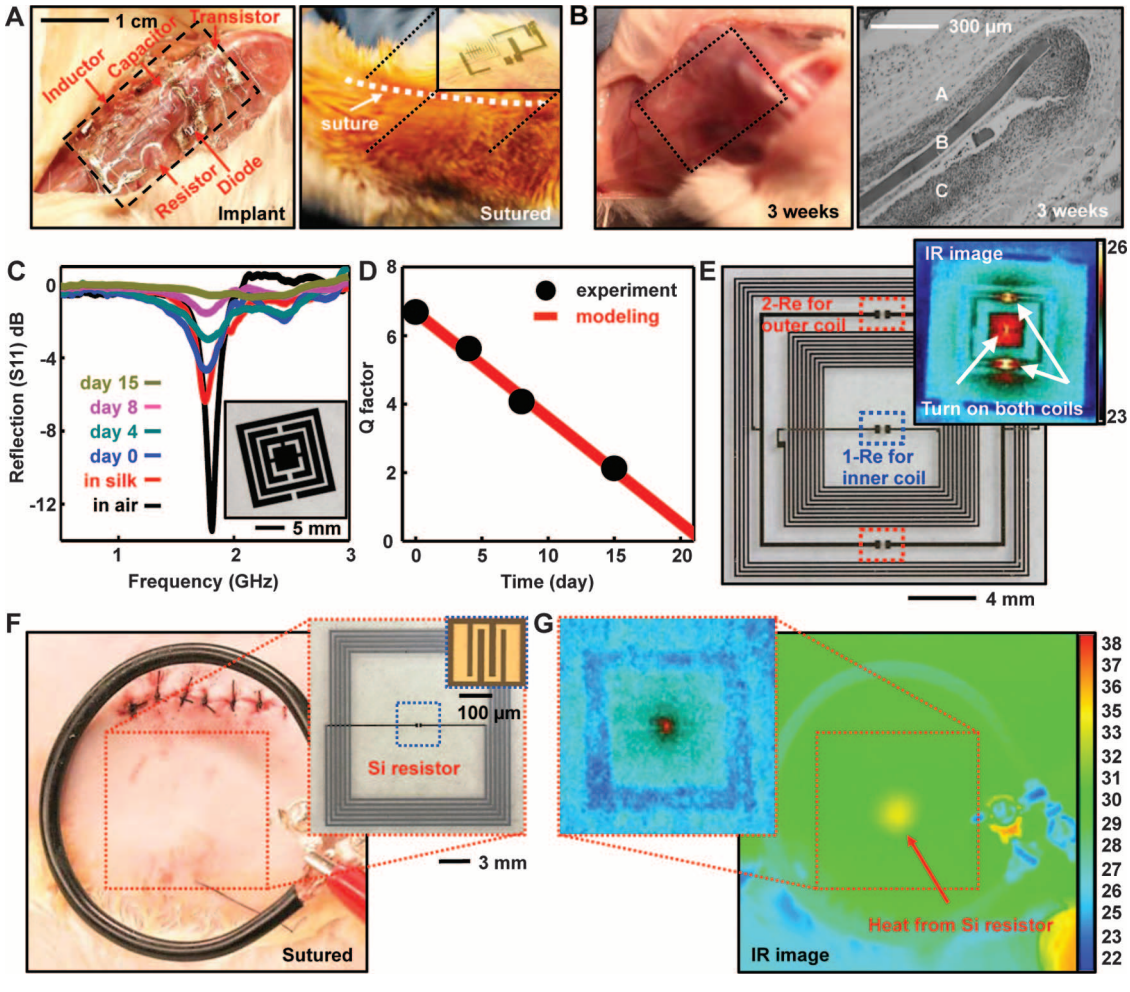

Fig. 4. In vivo evaluations and example of a transient bioresorbable device for thermal therapy. (**A**) Images of an implanted (left) and sutured (right) demonstration platform for transient electronics located in the subdermal dorsal region of a BALB/c mouse. (**B**) Implant site after 3 weeks (left). (Right) Histological section of tissue at the implant site, excised after 3 weeks, showing a partially resorbed region of the silk film. (A, subcutaneous tissue; B, silk film; C, muscle layer). (**C**) Resonant responses of an implanted transient rf metamaterial structure before and after placement in a silk package, immediately after implantation and at several time intervals thereafter. (**D**) Measured and calculated *Q* factor for the metamaterial. The results indicate transience dominated by the diffusion of biofluids through the silk package. (**E**) Transient wireless device for thermal therapy, consisting of two resistors (red outline) connected to a first wireless coil (70 MHz; outer coil) and a second resistor (blue outline) connected to a second, independently addressable, wireless coil (140 MHz; inner coil). The inset shows a thermal image of this device coupled with a primary coil operating at two frequencies, to drive both the inner and outer coils simultaneously. (**F**) Primary coil next to a sutured implant site for a transient thermal therapy device. The inset shows an image of a device. (**G**) Thermal image collected while wirelessly powering the device through the skin; the results show a hot spot (5°C above background) at the expected location, with a magnified view in the inset.

voltage for a given current output) and 0.23%/°C (percentage change in resistance), both of which are consistent with the behavior of conventional, nontransient devices (*15*). Ultrathin Si solar cells (~3 μm thick) provide fill factors of 66% and overall power conversion efficiencies of ~3%, even without light-trapping structures, backside reflectors, or antireflection coatings. Doped Si NMs can serve as strain gauges (Fig. 3E, left), with gauge factors of nearly ~40 (Fig. 3F, left, and fig. S10B), which are comparable to those of state-of-the art devices (*16*). As an example of interconnected components, we built a transient digital imaging system, consisting of collections of Si NM photodiodes with blocking diodes for passive matrix addressing (Fig. 3E, right), capable of capturing pictures when operated in a scanned mode (Fig. 3F, right, and fig. S10D). (See more details on device dimensions in fig. S11.) The yield here is >90% [i.e., 58 out of 64 pixels were fully functional (fig. S12)]. One possibility for power supply involves Si solar cells such as those shown in fig. S10A. Another uses inductors and capacitors like those in Figs. 1A and 3A and fig. S9 as wireless antennas for near-field mutual inductance coupling to separately powered, external primary coils. This option is interesting for implantable devices (*4*), made possible by the biocompatibility of the constituent materials (Fig. 1), as established in unrelated contexts (*6*).

To demonstrate opportunities, we conducted a series of in vivo and in vitro experiments. Various representative transient devices were fabricated, sealed in silk packages, sterilized with ethylene oxide, and then implanted in the subdermal region of BALB/c mice in accordance with Institutional Animal Care and Use Committee protocols. Figure 4A shows the case of the platform in Fig. 1. Examination after 3 weeks (Fig. 4B, left) revealed only faint residues, with evidence of slow reintegration into the subdermal layers, along with apparent revascularization. The histological section in Fig. 4B (right) shows the subdermal layer (A), the silk film (B), and the muscle layer (C) and reveals no significant inflammatory reactions. Additional analysis appears in fig. S13.

Inductive coils of Mg combined with resistive microheaters of doped Si NMs, integrated on silk substrates and housed in silk packages, can provide transient thermal therapy to control surgical site infections (*17*, *18*) as a nonantibiotic, programmable bacteriocidal appliqué that disappears as the patient moves beyond the period of greatest risk. In vitro tests demonstrate the efficacy of this approach (*6*). Figure 4, C and D, present a metamaterial rf antenna, as a generalized component for such a device, capable of continuous wireless monitoring after implantation. The data indicate transient behavior associated with the slow diffusion of biofluids through the edges of the silk package, with a measured quality (Q) factor that has time dependence consistent with theoretical models (*6*). Figure 4E shows an image of a functional device formed on glass that includes two coils with different resonance frequencies (~70 and ~140 MHz) and three separate heaters. Wirelessly operating either or both of these coils with appropriate frequencies and power levels applied to a separate primary coil enables full control of the system, as illustrated in the thermal image in the inset. (See figs. S14 to S16 for other examples.) To illustrate in vivo functionality, a fully transient version of this device was implanted under the skin of a Sprague-Dawley rat (Fig. 4F). Inductive coupling through the skin generates a localized temperature increase of ΔT ~5°C (Fig. 4G), coincident with the position of the heater. The functional transience has a time scale of 15 days, chosen via the crystallinity of the silk, to coincide with the most critical period, which is the first few days after an operation, to sterilize and maintain asepsis at the wound site. After this time, the device disappears, leaving only remnants of silk, which resorb on longer time scales, to eliminate the long-term burden associated with additional exogenous implant material.

Concepts reported here establish a baseline of materials, modeling approaches, manufacturing schemes, and device designs for transient electronic systems, sensors, actuators, and power supplies. The Si NMs are critically important elements, because their use enables sophisticated semiconductor components with both active and passive functionality. For the dielectrics and conductors, additional possibilities range from collagen to poly(lactic-co-glycolic acid) and from iron to zinc, respectively. Alternative modes of transience include absorption, corrosion, and depolymerization. The rates for these processes could, conceivably, be adjustable in real time and/or sensitive to the properties of the surrounding environment, determined by chemical or biological events, or changes in temperature, pressure, or light. Combining such possibilities in transience with ideas in soft, tissue-like electronics will further expand opportunities for applications in biomedical devices (*7*).

References and Notes

1. C. J. Bettinger, Z. Bao, *Adv. Mater.* **22**, 651 (2010).
2. M. Irimia-Vladu *et al.*, *Adv. Funct. Mater.* **20**, 4069 (2010).
3. C. Legnani *et al.*, *Thin Solid Films* **517**, 1016 (2008).
4. D.-H. Kim *et al.*, *Nat. Mater.* **9**, 511 (2010).
5. Y. Wang *et al.*, *Biomaterials* **29**, 3415 (2008).
6. Information on materials and methods is available in the supplementary materials on *Science* Online.
7. D.-H. Kim *et al.*, *Science* **333**, 838 (2011).
8. R. K. Iler, *J. Colloid Interface Sci.* **43**, 399 (1973).
9. J. D. Rimstidt, H. L. Barnes, *Geochim. Cosmochim. Acta* **44**, 1683 (1980).
10. M. Morita, T. Ohmi, E. Hasegawa, M. Kawakami, M. Ohwada, *J. Appl. Phys.* **68**, 1272 (1990).
11. H. Seidel, L. Csepregi, A. Heuberger, H. Baumgartel, *J. Electrochem. Soc.* **137**, 3612 (1990).
12. R. D. Levine, *Molecular Reaction Dynamics* (Cambridge Univ. Press, Cambridge, 2005).
13. X. Hu *et al.*, *Biomacromolecules* **12**, 1686 (2011).
14. H.-J. Chung *et al.*, *Adv. Funct. Mater.* **21**, 3029 (2011).
15. S. Santra, P. K. Guha, S. Z. Ali, I. Haneef, F. Udrea, *IEEE Sens. J.* **10**, 997 (2010).
16. S. M. Won *et al.*, *IEEE Trans. Electron Devices* **58**, 4074 (2011).
17. *Am. J. Infect. Control* **24**, 380 (1996).
18. D. J. Anderson *et al.*, *PLoS ONE* **4**, 1 (2009); http://dx.doi.org/10.1371/journal.pone.0008305.

Acknowledgments: The work on materials, integration schemes, manufacturing approaches, and design strategies was supported by the Defense Advanced Research Projects Agency. The theoretical analysis and associated experiments were supported by an NSF INSPIRE grant. The techniques for creating and manipulating Si nanomembranes were developed in work supported by an Air Force Office of Scientific Research Multi University Research Initiative program. The animal studies were funded by the National Institutes of Health (grant EB002520). The facilities for characterization and analysis were provided by the Material Research Laboratory and Center for Microanalysis of Materials at the University of Illinois at Urbana–Champaign, both of which are supported by the U.S. Department of Energy.

Supplementary Materials

www.sciencemag.org/cgi/content/full/337/6102/1640/DC1
Materials and Methods
Figs. S1 to S22
References (*19*–*32*)

19 June 2012; accepted 29 August 2012
10.1126/science.1226325

Gold-Catalyzed Direct Arylation

Liam T. Ball, Guy C. Lloyd-Jones,* Christopher A. Russell*

Biaryls (two directly connected aromatic rings, Ar^1-Ar^2) are common motifs in pharmaceuticals, agrochemicals, and organic materials. Current methods for establishing the Ar^1-Ar^2 bond are dominated by the cross-coupling of aryl halides (Ar^1-X) with aryl metallics (Ar^2-M). We report that, in the presence of 1 to 2 mole percent of a gold catalyst and a mild oxidant, a wide range of arenes (Ar^1-H) undergo site-selective arylation by arylsilanes (Ar^2-$SiMe_3$) to generate biaryls (Ar^1-Ar^2), with little or no homocoupling (Ar^1-Ar^1/Ar^2-Ar^2). Catalysis proceeds at room temperature and tolerates a broad range of functional groups, including those incompatible with cross-coupling. These features expedite biaryl preparation, as demonstrated by synthesis of the nonsteroidal anti-inflammatory diflunisal.

The biaryl moiety (two directly connected aromatic rings, Ar^1-Ar^2) is a common functionality in pharmaceuticals [such as Lipitor, Crestor, and Diovan, three of the most widely prescribed drugs in 2010 (*1*)]; in agrochemicals; and in many modern organic materials, including liquid crystal displays, light-emitting diodes, and conducting polymers. The